

UDC 620.91

**SOLID OXIDE FUEL CELL STACK SIMULATION USING EFFECTIVE MEDIUM APPROXIMATION****A.U. Sharafutdinov, Yu.S. Fedotov, S.I. Bredikhin**

*Institute of Solid State Physics RAS,  
142432, Russia, Chernogolovka, Moscow region, Academician Ossipyan, 2,  
e-mail: [shazat@issp.ac.ru](mailto:shazat@issp.ac.ru)*

*Received 28.05.2019**Accepted 11.08.2020*

*NiO/10Sc1CeSZ/LSM membrane-electrode assembly (MEA) was prepared using screen printing technology. A series of current-voltage characteristics was measured. Using experimental data a numerical model of SOFC stack was composed in COMSOL Multiphysics finite element analysis software. Distributions of temperature, reactants concentrations, gas pressures and velocities were calculated using the effective media approximation. Comparing the results with known theoretical observations revealed that the effective media approximation allows one to simulate the SOFC stack behavior adequately and reduce corresponding computational mesh size by a factor of  $10^1$ – $10^3$  depending the stack size. It was found that high heat exchange efficiency at the stack microchannels suppresses the dependence of temperature variation amplitude in the reaction zone on the input airflow temperature. This allows one to lower both the rate of input airflow and its temperature avoiding significant growth of temperature gradients across the stack.*

**Keywords:** SOFC, COMSOL, electrolyte-supported cell, fuel cell stack, computational fluid dynamics, effective medium.

**DOI:** 10.32737/2221-8688-2020-3-298-314

**Introduction**

Over recent decades the developed countries have made many efforts to reduce the percentage of traditional energy sources in overall energy balance as well as to increase the energy efficiency. The solid oxide fuel cells technology has great potential in the field due to high energy efficiency and purity compared to traditional ones. It bases on the galvanic process, in which the electrolyte is solid, conducts only  $O^{2-}$  and forms a membrane between the oxidizer, typically air, from the one side and fuel gas from the other side. The process at the electrodes takes place as long as air and fuel gas are separately fed to the cell. As a result the cell produces the electrical energy, heat, steam and  $CO_2$ . The working temperature of such devices varies in the range 600–900°C depending on the materials and structure used [1]. As for the fuel, it may be either pure hydrogen or syngas, a product of hydrocarbons complete or partial reforming, containing  $H_2$ ,

CO and a certain amount of  $CH_4$ . Electrochemical fuel oxidation at denoted temperatures does not lead to formation of poisonous nitrogen oxides in contrast with conventional fuel combustion. The efficiency of the cell is limited not by the Carnot cycle but by the oxidation Gibbs free energy divided by the heat of combustion [2]. Hence, the energy efficiency for natural gas can potentially reach 70%, which is extremely rewarding.

The fuel cell always contains three main parts: an electrolyte membrane and two electrodes, an anode at the fuel side and a cathode at the air side. Therefore, the cell is often named membrane-electrode assembly (MEA) to distinguish a certain item from the technology name. The typical operating voltage of a cell is 0.7–0.8 V, typical current density 0.2–1 A/cm<sup>2</sup>. MEAs differ in geometry and mechanical support. The main geometry types are planar and tubular [3] while the supporting

role may be assigned to either the electrolyte membrane, anode, cathode or special external layer [4]. In this paper we focus on the planar electrolyte-supported cells (ESC) since they are developed in ISSP RAS. For energy production the MEAs are combined into stacks containing 20–60 pieces. It leads to multiplying the voltage up to values suitable for a practical use. Cell stacking allows one to reach high power densities minimizing current collecting and gas supply subsystems (up to 2.5 kW/kg, [5, 6]). High power densities require effective cooling of the stack, e.g. by the excess amount of air. Additional effort is also required to lower temperature gradients across the stack as the power density grows. Therefore the questions of air cooling and uniform gas distribution in the fuel cell stacks are still the focal point of analytical, numerical and experimental studies [7, 8].

In the adiabatic standalone operating mode of SOFC stack the major sources of the thermal gradients are non-uniform current distribution due to fuel exhaustion and non-uniform heat exchange with inflow air [9]. In [10] it was shown that using the co-flow design one can choose the optimal temperature and flow rate of input air flux in such a way that these thermal features partially compensate each other.

Any fuel cell stack contains a set of small-scale structures: the microchannels with 0.1-1 mm cross section dimensions and 0.01-0.5 mm thick MEA layers. An explicit account of these structures is expensive in the terms of computational cost.

One can reduce computational mesh size

$$\frac{\nabla P}{\rho} + \tau p + (2 - \beta)u_h \nabla u_h = 0 \quad (1)$$

Here  $\tau$  is the wall shear stress and  $p$  is the header cross section perimeter,  $u_h$  is the axial flow velocity,  $\beta$  is defined as follows: the axial component of flow velocity at the entrance of

$$\frac{\nabla(P_{in} - P_{out})}{\rho} + (\tau_{in} p_{in} + \tau_{out} p_{out}) + (2 - \beta_{in} - (2 - \beta_{out}) \frac{A_{out}^2}{A_{in}^2}) u_{h,in} \nabla u_{h,in} = 0 \quad (2)$$

Here  $A_{in/out}$  is the cross-sectional area of input/output header (see **Fig. 1**).

It is worth noting that the pressure drop in a microchannel  $P_{in} - P_{out} = \Delta P_f + \Delta P_{hc}$  is

by a factor of  $10^1$ - $10^3$  (depending on the stack size) imitating the small-scale structures by properly designed continuous media. Definitely, such an "effective media" approximation must be validated. Generally, the widths of current collector ribs and microchannels are small enough to neglect the oscillations of the temperature and reactants concentrations within one period of the microchannel structure. However, the applicability of the method to the flow and pressure distributions is in question. Since the heat, electrical and gas flow problems are closely connected, errors rooted in one phenomenon simulation extend to the others. To maintain uniform chemical and thermal conditions one should keep the gas flows uniform across the stack. In [11] an influence of gas supply unequal in stacking direction was investigated. The authors demonstrated that unequal fuel distribution across the stack enhances the current distribution inhomogeneities, whereas unequal air supply influences primarily the temperature distribution.

Let us summarize known experimentally verified results on gas distribution in fuel cell stacks for the subsequent comparison with our simulation results. The air and fuel flows in microchannels of the stack are normally laminar and can be described by Poiseuille equation, whereas the flows in the distribution headers and pipelines can be either laminar, turbulent or transitional [12]. To get the flow distribution in the headers of the stack one can base on the momentum conservation law (MCL) [12, 13]:

microchannel is equal to  $\beta u_h$ . Pressure and velocity distributions are assumed to be averaged in the flow cross section. Thus, the pressure drop in the microchannels is determined by the following equation:

determined by the viscous friction term  $\Delta P_f$  and the header-microchannel transition losses

$\Delta P_{hc}$ . The latter is due to abrupt flow expansion/contraction and 90° turning of the

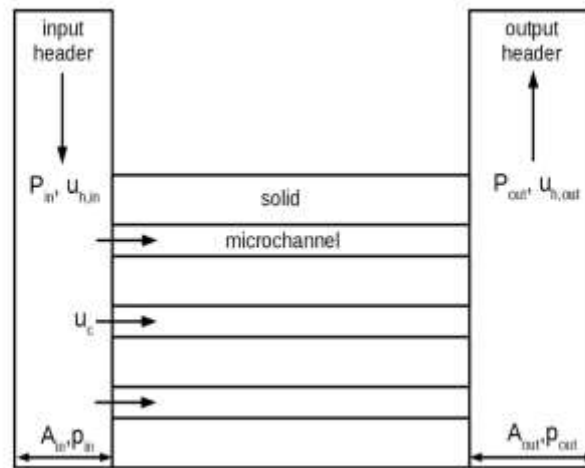


Fig. 1. Schematic diagram of the gas distribution subsystem.

The exact analytical solution of the last equation has been found in [14] in an assumption that the wall shear stress is given by Darcy–Weisbach formula  $\tau = f \rho u_h^2 / 8$  and the factor  $f$  is independent of the gas velocity  $u_h$ .

$$\frac{\nabla(P_{in} - P_{out})}{\rho} + (2 - \beta_{in} - (2 - \beta_{out}) \frac{A_{in}^2}{A_{out}^2}) u_{h,in} \nabla u_{h,in} = 0 \quad (3)$$

In this limit the pressure in the input header grows from the entrance to the interior of the stack due to the pressure recovery phenomenon. But the recovery is not complete since the fraction  $\beta_{in}$  of gas slows down by reaction forces in the microchannels rather than by the pressure gradient. This picture has been confirmed experimentally in [15].

Formation of large-scale vortices leads to additional suppression of the pressure recovery in the input header [8]. The  $\beta$  coefficients depend on the header/microchannel

Typically the air pressure distribution in the headers is determined by the inertia rather than by the viscous friction. Neglecting viscous friction terms the authors of [13] have solved the following equation:

cross-sectional area ratio, flow velocities ratio and distance between microchannels [16]. As the microchannels flow velocity exceeds that of the header flow  $\beta_{out}$  tends to negative values [16]. At a very large velocity of the microchannels flow an unstable jets formation begins in the output header [17].

The opposite limit of low volumetric flows has been considered in [18, 19]. In this case the pressure distribution is determined by viscous friction and the MCL (see Eq. 2) takes the following form

$$\frac{\nabla(P_{in} - P_{out})}{\rho} + (\tau_{in} p_{in} + \tau_{out} p_{out}) = 0 \quad (4)$$

### Purpose of the article

In this paper we present the three-dimensional multiphysics model of SOFC stack based on computational cost-saving method of effective medium. According to the method we replace layered structures of the stack by continuous media with anisotropic properties.

We compare the results of such approach with the known MCL-based theoretical and experimental results for the pressure distribution in the fuel cell stacks and list the applicability limits of the effective media method.

### Experimental part

Electrolyte-supported MEA was made by electrode deposition on a ceramic electrolyte plate using screen printing technique. Plates of ceramic electrolyte were prepared in the following sequence: 1) preparation of a ceramic slurry 2) ceramic tape casting 3) tape drying 4) lamination of stacks 5) removing bundles 6) sintering [20]. Electrolyte gains mechanical stability during the sintering process at 1500 °C. At this temperature the density of resulting electrolyte is maximal. Chemical composition of electrolyte was as follows: 10%Sc<sub>2</sub>O<sub>3</sub> 1%CeO<sub>2</sub> 89%ZrO<sub>2</sub>, the thickness was 250 μm. The anode and cathode were deposited by screen printing technique followed by sintering.

HERAEUS V-006 was used as a binder for screen printing pastes. Both electrodes were built in two layers: functional and current collection layer. The anode functional layer of 15 μm thickness consisted of 40 wt.% NiO and 60 wt.% 10Sc1CeSZ. The anode current collection layer (ACCL) of 30 μm thickness contained 60 wt.% NiO and 40 wt.%

10Sc1CeSZ. After anode deposition the plate was fired at 1380 °C. Then the cathode was deposited. The cathode functional layer of 15 μm thickness contained 60 wt.% (La<sub>0.8</sub>Sr<sub>0.2</sub>)<sub>0.95</sub>MnO<sub>3</sub> and 40 wt.% 10Sc1CeSZ. The cathode current collection layer (CCCL) of 30 μm thickness consisted of pure (La<sub>0.8</sub>Sr<sub>0.2</sub>)<sub>0.95</sub>MnO<sub>3</sub>. After cathode deposition the plate was fired at 1100 °C.

Current-voltage characteristics were measured on a button cell of 21 mm diameter.

Four-probe method was applied for the measurement using potentiostat/galvanostat. Platinum mesh and wiring were used to connect MEA to potentiostat/galvanostat [21]. Air and fuel flow rates were high enough to assume uniform concentrations of chemical species across the button cell surface.

The aforementioned characteristics provide us enough information on electrochemical transport to build a numerical model of the fuel cells stack based on this MEA.

### NUMERICAL MODEL

Nomenclature	
$R$	Universal gas constant
$F$	Faradey constant
$T$	Temperature
$\vec{q}$	Heat flow
$j$	Density of electronic current
$\vec{u}_g$	Effective gas flow speed (here and further index $g$ stands for air or fuel)
$\rho_g$	Density of gas $g$
$\mu_g$	Dynamic viscosity of gas $g$
$p_i$	Pressure of gas specie $i$
$h_l$	Height of layer corresponding to one SOFC in stack
$k_p$	Thermal conductivity matrix of effective body

#### 1. Geometric setup

The model is composed in COMSOL Multiphysics finite-element analysis software [22] based on the prototype crossflow SOFC

stack design, which is being developed in ISSP RAS. The model consists of SOFC stack, air and fuel supply pipes and thermal insulation.

A stack consists of 34 MEAs alternated with Crofer 22APU steel interconnects (

**Fig. 2**) and high-temperature glass-ceramic sealing compound [23]. The stack is compressed between two thick 20 mm Crofer 22APU steel plates to ensure sealing.

Reactants reach the MEA electrodes through the microchannels milled on the plates surface. The channels width is small enough to

assume lossless current collection (**Table 1**).

According to the effective medium approach we do not define the channels explicitly in our model. Instead, we divide the stack into effective media domains describing the layered structure in terms of averaged parameters such as porosity, anisotropic thermal and electric conductivities etc.

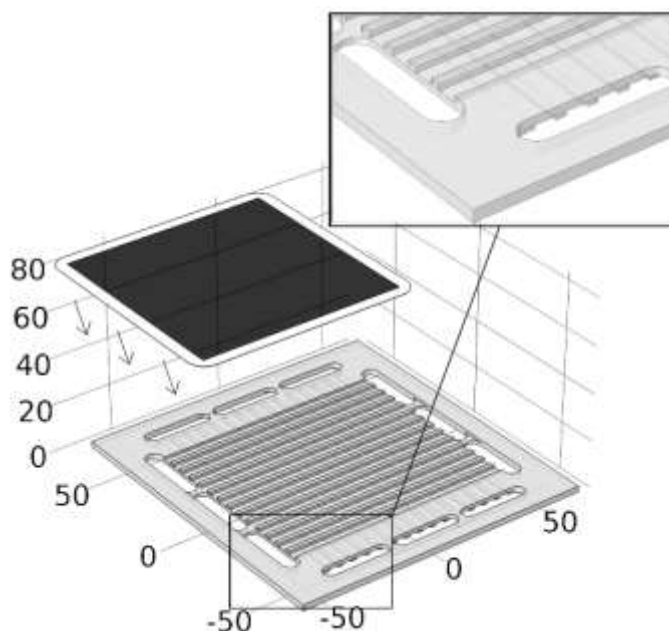


**Fig. 2.** Membrane electrode assembly and interconnect plate. The width and depth of the microchannels are doubled for visualization. All dimensions are in millimeters.

**Table 1.** Dimensions of key components of the reaction zone

Stack component	Thickness/Width
Glass-ceramic sealing	150 $\mu\text{m}$
Steel interconnect	2,3 mm
Electrolyte membrane	250 $\mu\text{m}$
Electrodes	45 $\mu\text{m}$
Air channels	0,8 mm/2 mm
Fuel channels	0,4 mm/2 mm

Thus, we have virtual media of six types: 1 – reaction zone; 2 – gas distributor; 3 – stiffening bridges; 4 – outer frame; 5 – end

plates (**Fig. 3**); 6 – air and fuel distribution headers (suppressed notches).

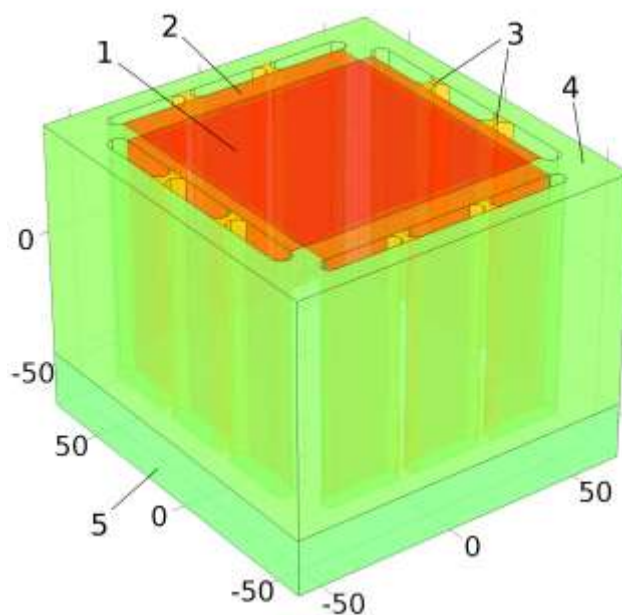


**Fig. 3.** Stack with domains of various virtual media denoted. All dimensions are in millimeters.

Air and fuel supply lines were assumed to be welded to the upper end plate (see **Fig. 4**). Parameters of PROMALIGHT-1000X have been used to model 50 mm-thick thermal insulation.

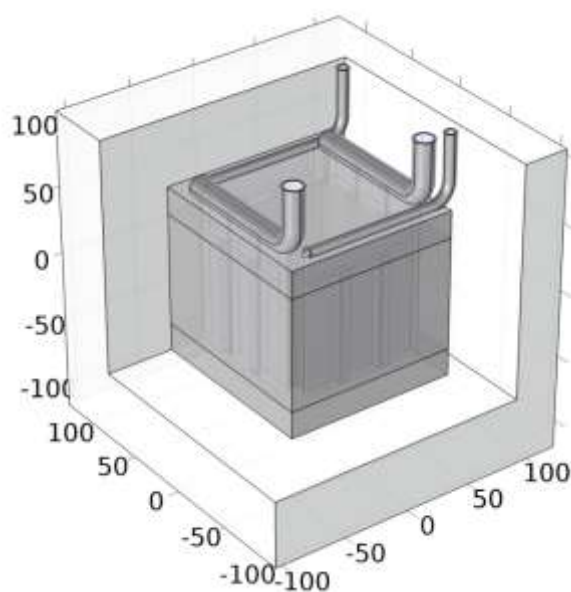


**Fig. 4.** Outline of the full model. The frontal part of insulation is hidden. All dimensions are in millimeters.

## 2. Physical model

### A. Heat transfer

The temperature distribution is given by the heat equation in porous media:

$$\sum_g \rho_g C_p^g \vec{u}_g \cdot \nabla T + \nabla \cdot \vec{q} = Q_v \quad (5)$$

$$\vec{q} = -k_p \nabla T \quad (6)$$

Here summation (index  $g$ ) runs over gases flowing through the effective medium – air or fuel.  $Q_v$  stands for heat dissipation resulting from reaction heat and ohmic heating.  $C_p^g$  is specific heat of gas flowing through the

channels. The thermal output of the hydrogen oxidation reaction is proportional to the current density in MEA and entropy change during the reaction:

$$Q_r = \frac{-j}{2F} T \Delta S \equiv j U_q \quad (7)$$

Using the tabulated values of entropy change during hydrogen oxidation, the values of  $U_q$  were found at 1000 K, 1100 K и 1200 K. Then we linearly interpolated  $U_q$ :

$$U_q = -0,0282[V] + 3,15 \times 10^{-4} [V/K] T - \frac{RT}{2F} \ln \left( \frac{P_{H_2}}{P_{H_2O}} \sqrt{\frac{P_{O_2}}{P_0}} \right) \quad (8)$$

The specific heat of gas mixtures was calculated as an average specific heat of components weighted by mass fractions. One can neglect the heat conductivity of gases in porous media in comparison with that of the

steel plates. The heat conductivity matrix  $k_p$  is anisotropic in virtual media 1, 2, 3 and 4 due to the laminated structure of the stack and presence of gas channels (

**Table 2).**

**Table 2.** Components of thermal conductivity matrix ( $\frac{W}{mK}$ ) at 780 °C.

	$k_p^{xx}$	$k_p^{yy}$	$k_p^{zz}$
Reaction zone	14,8	13,5	9,0
Air distributor	18,3	16,0	8,5
Fuel distributor	19,5	20,4	9,6
Stiffening bridges (air)	16,1	16,1	0,1
Stiffening bridges (fuel)	20,0	20,0	0,1
Outer frame	23,9	23,9	10,9

Surface-to-surface radiative heat transfer was accounted for within the manifolds.

### B. Charge transfer

The distribution of electric current is defined by the charge conservation law

$$\nabla \cdot j = 0, \quad (9)$$

and electrochemical transport equations with anisotropic conductivity matrix:

$$j = -\sigma \frac{\nabla \tilde{\mu}}{z_{O^{2-}}} = -\sigma \left( \nabla \phi + \frac{U_{rev}}{h_l} \right). \quad (10)$$

Here  $\nabla \tilde{\mu}$  is the electrochemical potential [24],  $z_{O^{2-}}$  is the charge of  $O^{2-}$  ion ( $-2e$ ),  $U_{rev}$  is the output voltage of a single SOFC in open circuit regime.  $U_{rev}$  is defined by the local temperature and concentrations of reactants.

Due to nonlinear electrode kinetics the effective medium conductivity should generally depend on the current density. We obtained this dependence from experimental current-voltage characteristics (see **Fig. 5**).

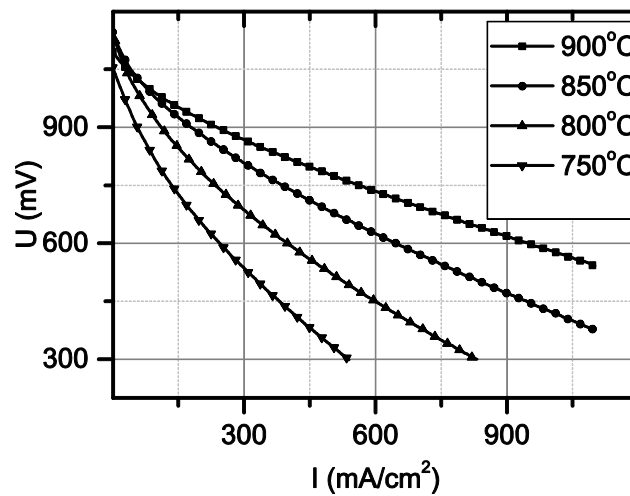


**Fig. 5.** Current voltage characteristics of ESC.

The current-voltage characteristics were fitted using the following approximation functions:

$$i = \frac{U}{B + A e^{-\frac{U}{b}}} \quad (11)$$

Here  $A$ ,  $B$  and  $b$  are fitting parameters depending on the temperature (see **Table 3**).

**Table 3.** Fitting parameters of the current-voltage characteristics

	800°C	850°C	900°C
A	2,87584	2,08166	1,29107
b	0,33113	0,23256	0,1548
B	0,54941	0,48132	0,37532

### C. Transfer of chemical species.

The equations stated in the next two sections are gas-specific, index  $g$  is omitted for brevity.

Fuel in the model is a mixture of  $H_2$  and

$H_2O$  while air is approximated as a mixture of  $N_2$  and  $O_2$ . To find the evolution of gas mixtures chemical composition across the stack we used the following equations:

$$\begin{aligned}\nabla \cdot \vec{j}_i + \rho(\vec{u} \cdot \nabla) \omega_i &= 0 \\ \vec{j}_i &= -\rho \omega_i \sum_k D_{ik} \vec{d}_k \\ \vec{d}_k &= \nabla x_k + \frac{1}{p} [(x_k - \omega_k) \nabla p] \\ x_k &= \frac{\omega_k}{M_k} M, M = \left( \sum_i \frac{\omega_i}{M_i} \right)^{-1}\end{aligned}\quad (12)$$

$\vec{j}_i$  – relative mass flux of the specie  $i$ .

$D_{ik}$  – Fick's diffusion coefficients

$\vec{d}_k$  – diffusional driving force

$x_k$  – mole fraction of the specie  $k$

$M_i$  – molar mass of the specie  $i$ .

Gases are assumed to obey the ideal gas equation of state:

$$\rho = \frac{p}{RT} \sum_i x_i M_i \quad (13)$$

The dynamic viscosity of gases was calculated on the basis of molecular kinetic theory [25]:

$$\begin{aligned}\mu &= \sum_i \frac{x_i \mu_i}{\sum_j x_j \phi_{ij}} \\ \phi_{ij} &= \frac{\left[ 1 + \left( \frac{\mu_i}{\mu_j} \right)^{\frac{1}{2}} \left( \frac{M_j}{M_i} \right)^{\frac{1}{4}} \right]^2}{\left[ 8 \left( 1 + \frac{M_i}{M_j} \right) \right]^{\frac{1}{2}}}\end{aligned}\quad (14)$$

Here  $\mu_i$  stands for dynamic viscosity of specie  $i$ .

#### D. Fluid flow

The dynamics of air and fuel in the supply manifolds is governed by Navier-Stokes equations with inertial term:

$$\begin{aligned}\rho(\vec{u} \cdot \nabla) \vec{u} &= \nabla \cdot \left( -p \vec{l} + \mu (\nabla \vec{u} + (\nabla \vec{u})^T) - \frac{2}{3} \mu (\nabla \cdot \vec{u}) \vec{l} \right) \\ \nabla \cdot (\rho \vec{u}) &= 0\end{aligned}\quad (15)$$

In the reaction zone and gas distributors one can neglect all dissipative terms except wall friction:

$$\begin{aligned}\nabla \cdot (-p\vec{l}) &= \mu k^{-1} \vec{u} \\ \nabla \cdot \vec{u} &= Q_v\end{aligned}\quad (16)$$

Here  $Q_v$  is the density of gas volume generation rate.  $k$  is the permeability of the corresponding virtual media.

### 3. Calculation details

A tetrahedral mesh with  $10^6$  elements was used to solve the computational model. The solution time to reach estimated relative error less than  $10^{-3}$  was about 2 hours with the server

based on Intel Xeon CPU-2630. For comparison the authors of [26] used  $1.6 \times 10^7$  elements to model a 30 times smaller stack.

### Results and discussion

A typical temperature distribution is presented on **Fig. 6**. One can observe an abrupt increase in the airflow temperature on the boundary between the input header and air distributor. This is due to high-efficiency heat

exchange in the shallow air channels of the distributor. To confirm this behavior we simulated the temperature distribution in a single air channel independently (see **Fig. 7**).

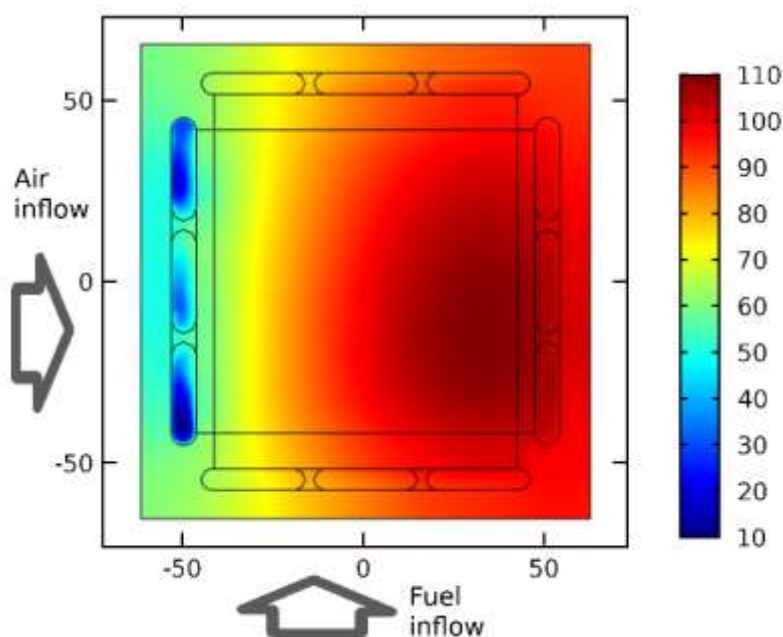


**Fig. 6.** Temperature distribution in the median section of the stack. The reference level is 780 °C. Voltage of 0.75 V on MEA, current 20 A, fuel utilization 65%. Fuel consists 97% H<sub>2</sub> 3% H<sub>2</sub>O.

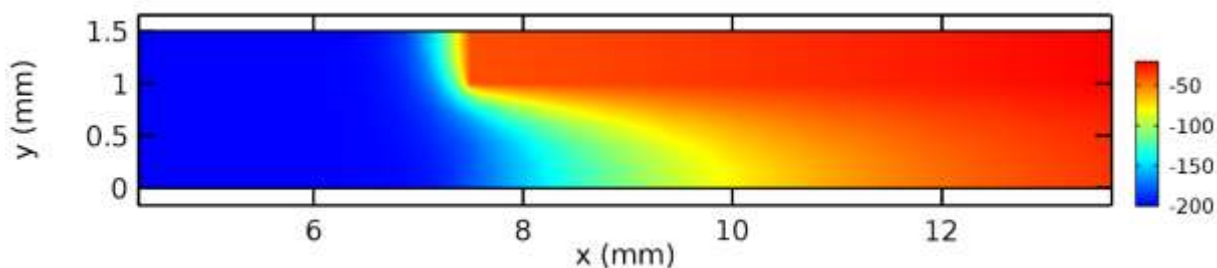


**Fig. 7.** Temperature distribution in one of the microchannels (half) of the air distributor in the cross-section parallel to the cell planes. Air flows from left to right, average air velocity in the channel – 3 m/s.

One can see that the temperature of input airflow equilibrates with the temperature of bipolar plate within a distance of 5 mm. Thus, one can assume the temperature of the air penetrating the stack to be equal to that of the cells. But the assumption that the cell entrance zone temperature is equal to the inlet gas temperature is in a sense impractical due to the aforementioned temperature jump [10]. Actually, this jump grows with the dissipated heat power at constant inlet air temperature. This fact leads us to interesting consequences.

Energy losses for air pumping through the stack depend severely on the airflow rate (**Fig. 8**). Hereby, lowering the temperature of input airflow one can use less air and therefore increase overall SOFC plant efficiency. But this

is limited by thermomechanical stresses causing cracks in ceramic MEAs and by the abrupt shrinkage of the power density in cold MEA zones. At glance, mainly the temperature difference between the hottest and the coldest points of the stack is equal to the air temperature difference, so lowering the air temperature should strongly increase the temperature gradients across the stack. However, our simulation shows that the range of temperature variation inside the stack grows much slower than the temperature difference between the output and input airflows (**Fig. 8**). Thus equating gas and solid temperature ranges can lead to excessive stack protection at the cost of efficiency.

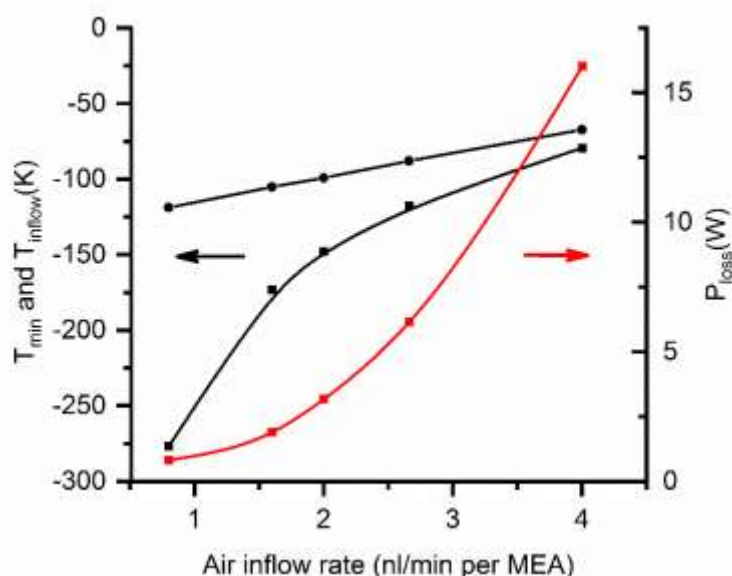


**Fig. 8.** Minimum temperature across the stack (black squares), air inflow temperature (black circles) and energy losses for pumping air through the stack (red squares) dependence on temperature difference between the air outflow and inflow. The average stack temperature and voltage on a single MEA are maintained 850°C and 0.75 V respectively. The diameter of the input air pipe  $d = 18\text{ mm}$ . The reference level is 850°C.

**Fig. 9** shows the dependence of the heat energy amount taken in the stack by air on the average air velocity in the air supply line. This curve was obtained by variation of the air pipes diameter keeping the volumetric air inflow rate constant. The red line corresponds to inevitable amount of energy needed to overcome viscous wall friction of air within the reaction zone and

air distributors channels. The additional losses grow as the flow velocity cubed (see **Fig. 9**). For small pipe diameters they are primarily caused by flow turning and expansion at the header entrance and exit. As the pipe cross section exceeds that of the header the pressure losses at the header-microchannel transition became dominant.

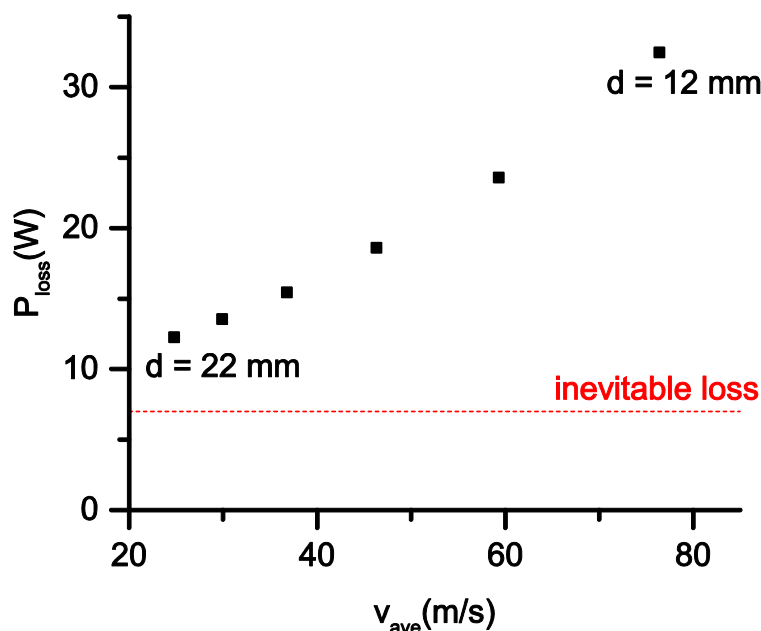


**Fig. 9.** The energy losses for pumping air through the stack on the average air velocity in the input air pipe. Here  $d$  is the diameter of the input air pipe.

Let us note that the cross-section averaged air pressure distribution along the exhaust header is close to parabolic one (see **Fig. 10**) as predicted by MCL (**Eq. 3**). However the approximation of uniform velocity distribution across the header cross section prevents from quantitative agreement with the theory: the normalization coefficients

$N = \langle u_h^2 \rangle / \langle u_h \rangle^2$  (in the notation of [15], where  $\langle \dots \rangle$  is averaging over the header cross section, should be introduced. When using the effective media approximation much attention should be paid to the flow boundary conditions on the interface between the headers and the stack interior.

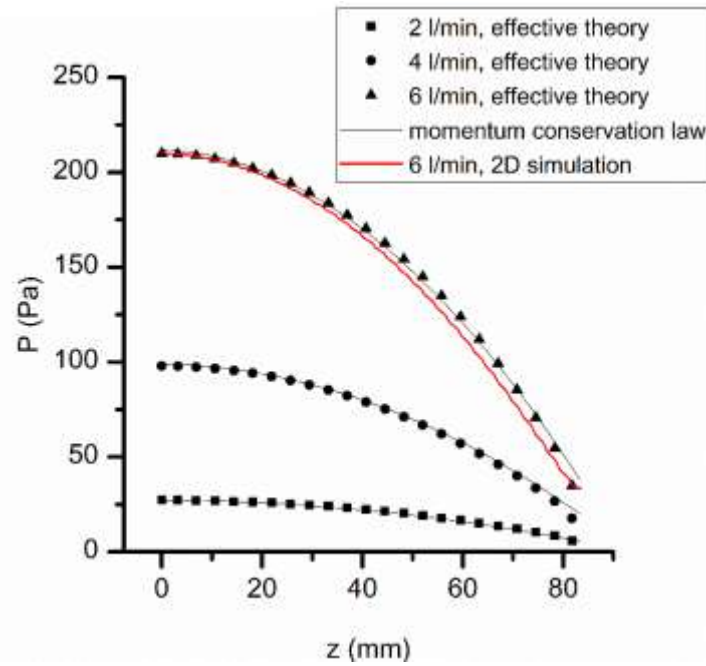


**Fig. 10.** Cross-section-averaged air pressure in the exhaust header on  $z$  for different air flows (the exit is on the right). Also the MCL results [13] with  $N = 1.2$  and the exact 2D simulation results are presented.

One can see (**Fig. 11**) that the inhomogeneity  $N$  grows with the microchannel/header flow velocities ratio  $u_c/u_h$ . In the notations of [13]  $\beta_{out}$  becomes more negative in the low flow velocity region of the exhaust header. This means that the effective media method leads to substantial errors in the velocity distribution in this region. However due

to low velocities in this region the pressure distribution is in reasonable agreement with exact simulation results (see **Fig. 10**).

Let us note that experimental values of  $N \cong 1.15 - 1.25$  from Fig 4 of [15] are close to the results of effective media simulation despite the scale differences.

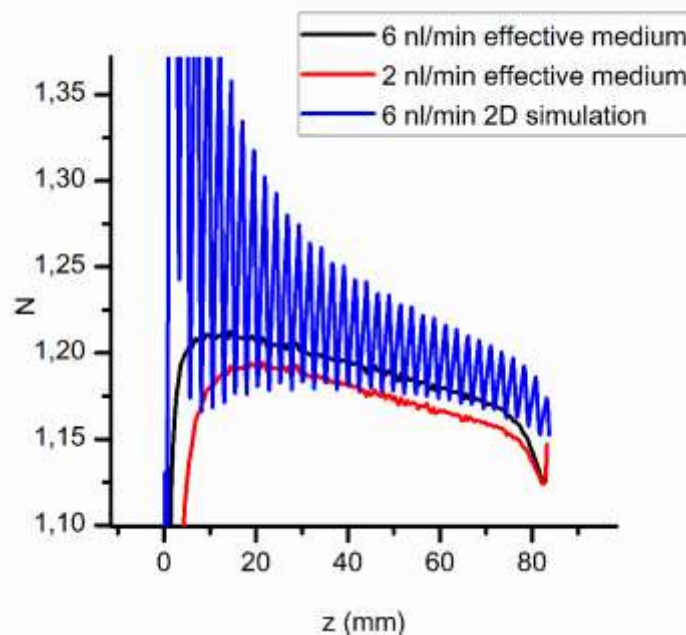


**Fig. 11.** The flow inhomogeneity coefficient  $N$  on  $z$ -coordinate for the effective medium method and exact 2D simulation in the exhaust header (the exit is on the right).

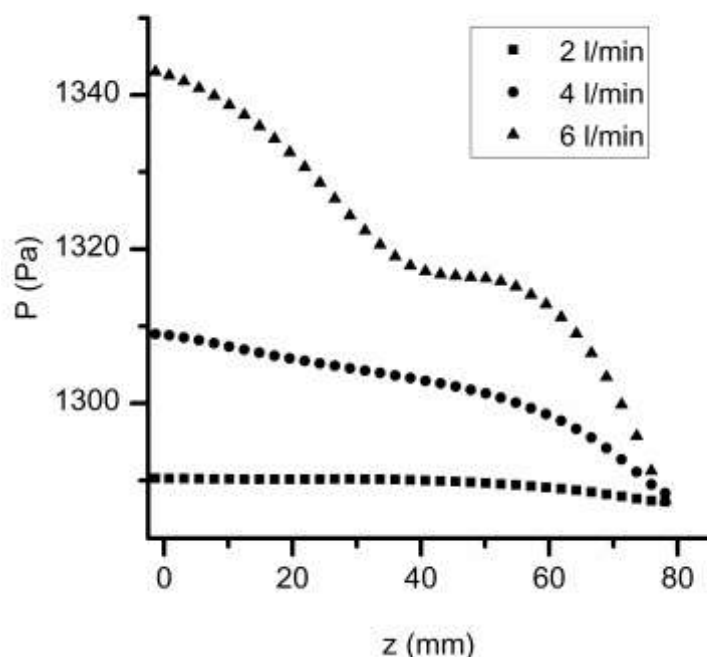


**Fig. 12.** The cross section averaged pressure on z-coordinate in the input header (the entrance is on the right).

One should account for the pressure drop in header-microchannel junctions  $\Delta P_{hc}$  by modification of boundary conditions in the effective media model. In the exhaust header an abrupt expansion occurs and one can use Borda-Carnot equation  $\Delta P_{hc}^{out} = \rho u_c^2 \beta (1 - \beta)$  where  $u_c$  is the microchannel flow velocity,  $\beta$  is the ratio of the channel and header cross sections. In the input header it is more difficult to find the pressure drop due to the combination of turning and expansion and due to the influence of the neighboring microchannels flow. The naive boundary condition of normal flow leads to overestimated pressure values in the inlet header since it assumes  $\beta_{in} = 0$ . Expressions for t-branching are not applicable, since the microchannel flows are not independent. Anyway the input pressure drop  $\Delta P_{hc}^{in}$  profile can be obtained using exact simulation of this part of the stack. This additional work should be attributed to the drawbacks of the effective media method.

Let us note that according to MCL [13] one can make the gas flow exactly uniform across the stack choosing the ratio of the exhaust and input header cross sections equal to  $\sqrt{2}$ . The uniformity is maintained for intermediate flow velocities – high enough for viscous friction to be negligible and low enough to prevent large-scale vortices formation in the input header (**Fig. 12**).

In the fuel headers the pressure distribution can be determined either by the viscous friction or by inertia depending on fuel composition. One can see from **Fig. 13** how the air recovery arises as the density of fuel grows. Thus it is impossible to make the fuel distribution uniform by geometrical-only means (see e.g. [27]) due to the natural fuel composition volatility during the stack operation. The pressure would be uniform only for the single working point implying certain temperature, fuel flow, current and stack quality.

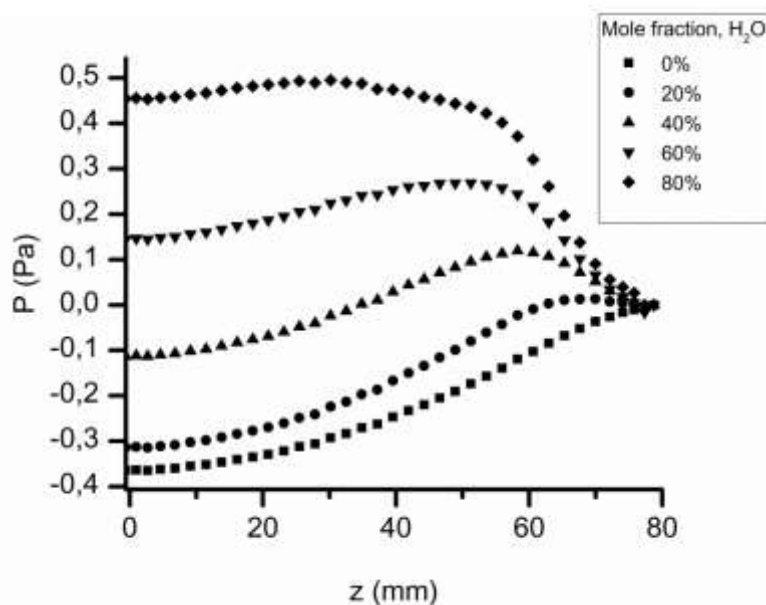


**Fig. 13.** Cross section-averaged pressure distribution in the input fuel header (the entrance is on the right).

### Conclusions

Electrolyte-supported SOFC was prepared in a form of a button cell 21 mm in diameter. A series of current-voltage characteristics was measured. Using the experimental data a numerical effective medium model of SOFC stack was composed. Distributions of temperature, reactants concentrations, gas pressure and velocity were calculated.

It was shown that the computational cost-saving effective medium approach yields an adequate modeling result for SOFC stack. The pressure deviation from exact model was less than 7% within the range of acceptable gas inflows.

The method allows to reduce the computational mesh size by a factor of  $10^1$ – $10^3$  depending on the stack size. The drawbacks of the method are mostly related to the flow distribution in the input header of the stack.

Simple boundary conditions generally lead to an overestimation of the average pressure in the input header.

To avoid additional air pumping losses one should choose the input air pipe sectional area close to that of the headers since the excess amount of kinetic energy is mainly lost for pressure recovery due to vortices formation and header-microchannel transition losses.

The simulation has shown that the dependence of temperature variation amplitude in the reaction zone on the input airflow temperature is weak, primarily due to high heat exchange efficiency in the stack gas distribution domains. This result allows using much colder air for stack cooling compared to the estimates based on equating inlet air and the lowest possible MEA temperatures.

*This work was supported by the Russian Science Foundation grant 17-79-30071 “Scientifically grounded optimization of power and mass-dimensional characteristics of planar SOFC stacks and development of fuel processor for highly-efficient transport and stationary power plants”. The gas dynamics numerical model of SOFC was developed under financial support of State Task of Institute of Solid State Physics RAS.*

### References

1. Isabella Burch J.G. A Survey on Global Activity to Phase Out Internal Combustion Engine Vehicles, Center for Climate Protection, 2018. <https://climateprotection.org/wp-content/uploads/2018/10/Survey-on-Global-Activities-to-Phase-Out-ICE-Vehicles-FINAL-Oct-3-2018.pdf>. Accessed 14-May-2019.
2. Tokyo Aims to Realize “Hydrogen Society” by 2020. *We Are Tomodachi*. 2016, vol. 14, pp. 24–25.
3. Minh N.Q., Takahashi T. Science and Technology of Ceramic Fuel Cells. Burlington, Elsevier, 1995, 379 p.
4. Vielstich W., Lamm A., Gasteiger H.A. Handbook of fuel cells. Chichester, Wiley, 2003, 488 p.
5. Bove R., Ubertini S. Modeling solid oxide fuel cells. Great Britain, Springer, 2008, 397 p.
6. Tucker M.C. Progress in metal-supported solid oxide fuel cells: A review. *J. Power Sources*. 2010, vol. 195, pp. 4570–4582.
7. Cable T.L., Sofie S.W. A symmetrical, planar SOFC design for NASA's high specific power density requirements. *Journal of Power Sources*. 2007, vol. 174, pp. 221–227.
8. Thomas L Cable, John A Setlock, Serene C Farmer. Method for making a fuel cell.
9. Ramadhani F., Hussain M.A., Mokhlis H., Hajimolana S. Optimization strategies for Solid Oxide Fuel Cell (SOFC) application: A literature survey. *Renewable Sustainable Energy Rev.* 2017, vol. 76, pp. 460–484.
10. Liu H.-H., Cheng C.-H., Hsueh K.-L., Hong C.-W. Modeling and design of air-side manifolds and measurement on an industrial 5-kW hydrogen fuel cell stack. *Int. J. Hydrogen Energy*. 2017, vol. 42, pp. 19216–19226.
11. Amiri A., Tang S., Vijay P., Tadé M.O. Planar Solid Oxide Fuel Cell Modeling and Optimization Targeting the Stack's Temperature Gradient Minimization. *Ind. Eng. Chem. Res.* 2016, vol. 55, pp. 7446–7455.
12. Inui Y., Ito N., Nakajima T., Urata A. Analytical investigation on cell temperature control method of planar solid oxide fuel cell. *Energy Convers. Manage.* 2006, vol. 47, pp. 2319–2328.
13. Yuan P. Effect of inlet flow maldistribution in the stacking direction on the performance of a solid oxide fuel cell stack. *Journal of Power Sources*. 2008, vol. 185, pp. 381–391.
14. Koh J.-H., Seo H.-K., Lee C.G., Yoo Y.-S., Lim H.C. Pressure and flow distribution in internal gas manifolds of a fuel-cell stack. *Journal of Power Sources*. 2003, vol. 115, pp. 54–65.
15. Bassiouny M.K., Martin H. Flow distribution and pressure drop in plate heat exchangers—I U-type arrangement. *Chem. Eng. Sci.* 1984, vol. 39, pp. 693–700.
16. WANG J. Pressure drop and flow distribution in parallel-channel configurations of fuel cells: U-type arrangement. *Int. J. Hydrogen Energy*. 2008, vol. 33, pp. 6339–6350.
17. Costamagna P., Arato E., Achenbach E., Reus U. Fluid dynamic study of fuel cell devices: simulation and experimental validation. *Journal of Power Sources*. 1994, vol. 52, pp. 243–249.
18. Bajura R.A. A Model for Flow Distribution in Manifolds. *Journal of Engineering for Power*. 1971, vol. 93, pp. 7–12.
19. Chernyavsky B., Sui P.C., Jou B.S., Djilali N. Turbulent flow in the distribution header of a PEM fuel cell stack. *Int. J. Hydrogen Energy*. 2011, vol. 36, pp. 7136–7151.
20. Maharudrayya S., Jayanti S., Deshpande A.P. Flow distribution and pressure drop in parallel-channel configurations of planar fuel cells. *Journal of Power Sources*. 2005, vol. 144, pp. 94–106.
21. Huang W.L., Zhu Q. Flow distribution in U-type layers or stacks of planar fuel cells. *Journal of Power Sources*. 2008, vol. 178, pp. 353–362.
22. Greco F., Frandsen H.L., Nakajo A., Madsen M.F., van herle J. Modelling the impact of creep on the probability of failure of a solid oxide fuel cell stack. *J. Eur. Ceram. Soc.* 2014, vol. 34, pp. 2695–2704.
23. Cheng H., Jing S., Xu Y., Deng Z., Li J., Li X. Control-oriented modeling analysis and optimization of planar solid oxide fuel cell system. *Int. J. Hydrogen Energy*. 2016, vol. 41, pp. 22285–22304.

24. Bao C., Wang Y., Feng D., Jiang Z., Zhang X. Macroscopic modeling of solid oxide fuel cell (SOFC) and model-based control of SOFC and gas turbine hybrid system. *Prog. Energy Combust. Sci.* 2018, vol. 66, pp. 83–140.
25. Burmistrov I., Agarkov D., Bredikhin S., Nepochatov Y., Tiunova O., Zadorozhnaya O. Multilayered Electrolyte-Supported SOFC Based on NEVZ-Ceramics Membrane. *ECS Trans.* 2013, vol. 57, pp. 917–923.
26. Burmistrov I., Drozhzhin O.A., Istomin S.Y., Sinitsyn V.V., Antipov E.V., Bredikhin S.I.  $\text{Sr}_{0.75}\text{Y}_{0.25}\text{Co}_{0.5}\text{Mn}_{0.5}\text{O}_{3-y}$  Perovskite Cathode for Solid Oxide Fuel Cells. *J. Electrochem. Soc.* 2009, vol. 156, p. B1212.
27. Dickinson E.J.F., Ekström H., Fontes E. COMSOL Multiphysics®: Finite element software for electrochemical analysis. A mini-review. *Electrochem. Commun.* 2014, vol. 40, pp. 71–74.
28. Sudaprasert K., Travis R.P., Martinez-Botas R.F. A Study of Temperature Distribution Across a Solid Oxide Fuel Cell Stack. *J. Fuel Cell Sci. Technol.* 2010, vol. 7, p. 11002.
29. Kharton V.V. Solid state electrochemistry. Weinheim, Chichester, Wiley-VCH, 2009–2011, 506 p.
30. Wilke C.R. A Viscosity Equation for Gas Mixtures. *J. Chem. Phys.* 1950, vol. 18, pp. 517–519.
31. Jackson J.M., Hupert M.L., Soper S.A. Discrete geometry optimization for reducing flow non-uniformity, asymmetry, and parasitic minor loss pressure drops in Z-type configurations of fuel cells. *Journal of Power Sources.* 2014, vol. 269, pp. 274–283.

## МУЛЬТИФИЗИЧЕСКОЕ МОДЕЛИРОВАНИЕ БАТАРЕИ ТВЕРДООКСИДНЫХ ТОПЛИВНЫХ ЭЛЕМЕНТОВ В ПРИБЛИЖЕНИИ ЭФФЕКТИВНОЙ СРЕДЫ

А.У. Шарафутдинов<sup>1</sup>, Ю.С. Федотов<sup>1</sup>, С.И. Бредихин<sup>1</sup>

Федеральное государственное бюджетное учреждение науки  
Институт физики твердого тела Российской академии наук,  
142432, Россия, Черноголовка, Московская область, Академика Осипьяна, 2,  
e-mail: shazat@issp.ac.ru

Мембранно-электродный блок (МЭБ)  $\text{NiO}/10\text{Sc}1\text{CeSZ}/\text{LSM}$  был изготовлен с помощью технологии трафаретной печати. Был измерен ряд вольт-амперных характеристик. По этим данным была построена численная модель батареи топливных элементов в ПО для конечно-элементных расчетов COMSOL Multiphysics. Были найдены распределения температур, концентраций реагентов, давления и скорости газов. Сравнением с теоретическими закономерностями показано, что метод эффективной среды позволяет адекватно моделировать поведение батареи топливных элементов, позволяя при этом снизить размер расчетной сетки в  $10^1$ – $10^3$  раз в зависимости от размера батареи. Было обнаружено, что высокая эффективность теплообмена в газораспределительных зонах батареи подавляет зависимость разброса температур в зоне реакции от температуры втекающего в батарею воздуха. Это позволяет понизить количество воздуха, используемого для охлаждения батареи, не увеличивая значительно градиентов температуры в батарее.

---

*Ключевые слова:* TOTЭ, COMSOL, электролит-поддерживающая ячейка, батарея TOTЭ, вычислительная гидродинамика, эффективная среда

***BƏRKOKSID YANACAQ BATAREYANIN EFFEKTİV MÜHİT ŞƏRAITI ÜÇÜN  
MULTİFİZİK MODELLEŞDİRİLMƏSİ***

***A.U. Şərəfuddinov, Yu.S. Fedotov, S.İ. Bredixin***

*Bərk cisimlərin fizikası institutu*

*142432, Rusiya, Çernoqolovka şəh., akad. Osipyan küç., 2; e-mail: shazat@issp.ac.ru*

*Bərkoksidi yanacaq batareyanın NiO/10Sc1CeSZ/LSM membran-elektrod bloku traforet çap usulu ilə hazırlanıb. Bir sıra volt-ampere xarakteristikaları təyin edilib və onlar əsasında yanacaq batareyanın rəqəmsal modeli yaradılıb. Temperaturun, reagentlərin qatılığının, qazların təzyiq və sürətinin paylanması müəyyən edilib. Göstərilib ki, effektiv mühit metodu yanacaq element batareyalarının işləmə rejimini adekvat modelləşdirməyə imkan verir.*

***Açar sözlər:*** *bərkoksidi yanacaq batareyaları, volt-ampere xarakteristikaları, membran-elektrod bloku, effektiv mühit metodu*